THE ASTROPHYSICAL JOURNAL, 565:1335–1347, 2002 February 1

MOTION OF FLARE FOOTPOINT EMISSION AND INFERRED ELECTRIC FIELD IN RECONNECTING CURRENT SHEETS

JIONG QIU, JEONGWOO LEE, DALE E. GARY, AND HAIMIN WANG
Center for Solar Research, Physics Department, New Jersey Institute of Technology, 323 Martin Luther King Boulevard, Newark, NJ 07102-1982; qiuj@plage.njit.edu
Received 2001 July 10; accepted 2001 October 1

ABSTRACT

A systematic motion of Hα kernels during solar flares can be regarded as the chromospheric signature of progressive magnetic reconnection in the corona, in that the magnetic field lines swept through by the kernel motion are those connected to the diffusion region at the reconnection point. In this paper, we present high-cadence and high-resolution Hα−1.3 Å observations of an impulsive flare that exhibits a systematic kernel motion and relate them to the reconnecting current sheet (RCS) in the corona. Through analyses of X-ray and microwave observations, we further examine the role of the macroscopic electric field inside the RCS in accelerating electrons. We measure the velocity of the kernel motion to be 20−100 km s^{-1}. This is used together with the longitudinal magnetic field to infer an electric field as high as 90 V cm^{-1} at the flare maximum. This event shows a special magnetic field configuration and motion pattern of Hα kernels, in that a light bridge divides a flare kernel into two parts that move in different manners: one moving into the stronger magnetic field and the other moving along the isogauss contour of the longitudinal magnetic field. The temporal variation of the electric field inferred from the former type of kernel motion is found to be correlated with 20–85 keV hard X-ray light curves during the rise of the major impulsive phase. This would support the scenario of magnetic energy release via current dissipation inside the RCS, along with the hypothesis of the DC electric field acceleration of X-ray–emitting electrons below 100 keV. However, there is no good temporal correlation between the hard X-ray emission and the inferred electric field from the other motion pattern. Furthermore, the microwave emission, which supposedly comes from higher energy electrons, shows a time profile and electron spectrum that differs from those of the X-ray bursts. We conclude that either the two-dimensional magnetic reconnection theory related to the Hα kernel motion is applicable to only some part of the flare region due to its special magnetic geometry, or the electron acceleration is dominated by other mechanisms depending on the electron energy.

Subject headings: Sun: activity — Sun: flares — Sun: magnetic fields

1. INTRODUCTION

Before the satellite era of solar observations, ground-based observations, particularly Hα observations, were extensively studied to gain understanding of solar flares. It is now well accepted that in most solar flares the magnetic reconnection and consequent energy release occur in the corona. The energy flux, either via thermal conduction or nonthermal electron precipitation, reaches the lower atmosphere and heats the chromosphere at a very short timescale, so the morphology of the flare in the chromosphere can be used to trace the coronal progress of magnetic energy release. The ever-advancing technology in recent years provides unprecedented high temporal and spatial resolutions in Hα observations (Wang et al. 2000; Raulin et al. 2000; Trottet et al. 2000; Kurt et al. 2000), which are valuable complements to satellite observations for a comprehensive understanding of solar flares.

Hα observations of solar flares, which usually look at the footpoint portion of the flare loops, have been used to infer the coronal magnetic energy release process for a particular type of flares, namely, dynamic flares (Švestka 1989). A most typical case of a dynamic flare is a two-ribbon flare, in which the two footpoint ribbons residing in opposite magnetic polarities are expanding outward and away from each other as the flare goes on (see a review by Švestka & Cliver 1992). It is now well recognized that the flare ribbon expansion is the chromospheric signature of the progressive magnetic reconnection in the corona in which new field lines reconnect at higher and higher altitudes. How quickly the ribbon expands in the chromosphere is then related to how fast the reconnection proceeds in the corona. Since the magnetic reconnection in the corona is hardly observable directly, many chromospheric observations have been conducted and analyzed in an effort to indirectly map the coronal magnetic reconnection (Schmieder et al. 1987; Švestka 1989; Falchi, Qiu & Cauzzi 1997).

Physically speaking, the velocity of the footpoint motion sweeping through the magnetic field lines corresponds to the rate of the magnetic flux convected into the diffusion region at the reconnection point in the corona where the reconnecting current sheet (RCS) is generated. Generation of the RCS is crucial in flare energy release because the free energy contained in the nonpotential magnetic field can be rapidly dissipated into heating the plasma and accelerating particles with the presence of the electric field. If we ignore the coronal electric field outside the RCS, a general measure of the rate of the magnetic reconnection, disregarding the details of the coronal magnetic field configuration, is the electric voltage drop φ_c along the RCS. This is related to the rate of the net change of the magnetic flux from one topological domain into another through the RCS by (Forbes & Lin 2000 and references therein)

$$\varphi_c = \int E_c \, dl = \frac{\partial \Phi_B}{\partial t} = \frac{\partial}{\partial t} \left(\int B_n \, da \right), \qquad (1)$$

where E_c is the local electric field strength, dl is the elemen-

tary length along the current sheet, Φ_B is the magnetic flux, B_n is the normal component of the magnetic field, and a is the newly brightened area swept through by the Hα kernel motion. In a two-ribbon flare case, dl is aligned in the direction of the ribbon, and the full length of the current sheet, which connects the two null points, is equal to the length of the ribbons. If neither the length of the ribbons nor the normal magnetic field changes with time significantly, equation (1) can be further written as

$$\varphi_c = \int V_{\parallel} B_n \, dl \, , \tag{2}$$

where $V_{\parallel}$ is the horizontal velocity of the ribbon expansion. Although equation (2) is derived for a two-ribbon flare case, its validity is not confined to such a particular magnetic configuration (Forbes & Lin 2000). However, it does contain a basic assumption that the motion observed in the chromosphere/photosphere depicts the motion of a separatrix along which the magnetic flux crosses the boundary between two topologically separated domains, i.e., a three-dimensional generalization of the two-dimensional concept of magnetic reconnection. In the case of a typical two-ribbon flare, the flare ribbons are the photospheric/chromospheric intersection of the separatrices dividing the open field line domain and closed field line domain. Because of the line-tying nature of the photospheric magnetic field, the motion of the ribbon should be regarded as a signature of the moving separatrix. If there is a translational symmetry along the ribbon, i.e., in a two-dimensional configuration, equations (1) and (2) are reduced to (Forbes & Priest 1984; Forbes & Lin 2000)

$$E_c = V_{\parallel} B_n \, , \tag{3}$$

yielding a measure of a uniform electric field strength along the current sheet. Using this relation, Poletto & Kopp (1986) derived the maximum $E_c \approx 2$ V cm^{-1} in a large two-ribbon flare.

We should emphasize that both the electric field strength, or voltage drop, and its evolution with time during the flare are important information that one can infer from chromospheric observations. The former can measure the amount of the magnetic energy that is available to fuel a flare, and the latter tells the progress of the magnetic reconnection, or the time profile of the reconnection rate. These can be further compared with the observed X-ray and microwave light curves, which give a measure of the flare particle acceleration. Since the MHD approach described above allows us to investigate the electric field only in a macroscopic scale, a sound interpretation of the comparative results further requires an appropriate model that describes how the plasma is energized by the electric field in the RCS. For instance, in the presence of a sufficiently large electric field with respect to the local Dreicer field (1959), electrons can be efficiently accelerated via the DC acceleration mechanism by either a sub-Dreicer field (Holman 1985; Benka & Holman 1994) or a super-Dreicer field (Litvinenko 1996; Litvinenko & Craig 2000). Given the electric field strength, some other important parameters of the RCS, as required by the acceleration theories, can be examined from comparison with observations. Therefore, a comparative study between the electric field in the RCS inferred from the flare footpoint motion and analyses of high-energy flare emission, namely, X-rays and microwaves, is particularly appealing for its potential in addressing a few important aspects of solar flare physics.

In the past, very few attempts have been made to explore the electric field in the RCS from the flare footpoint kernel motion (e.g., Poletto & Kopp 1986). These studies all involve two-ribbon flares whose configurations were conveniently approximated to a two-dimensional framework, and the role of the derived electric field in energizing the plasma was seldom reviewed. In this paper, we present analyses of multiwavelength observations of an impulsive flare which exhibits a systematic footpoint motion. The Hα observations taken at Big Bear Solar Observatory (BBSO) have an unprecedented high cadence (0.1 s) and high resolution (pixel size 0.″36) with excellent seeing conditions during the observation, which gives us a unique chance to follow the dynamical behavior of the flare and reliably obtain the time profiles of the footpoint motion. It is the very first attempt to explore the footpoint motion in the context of its relation to the RCS in a non–two-ribbon flare, and we will demonstrate that because of the particular configuration of this flare, it is appropriate to make a two-dimensional approximation and hence to derive an average electric field strength along the RCS. This is further compared with analyses of hard X-ray observations obtained from *Yohkoh* and microwave observations taken at Owens Valley Solar Array (OVSA) to understand the role of the electric field in accelerating the X-ray–and microwave-emitting electrons.

The paper is organized as follows: § 2 gives a brief overview of the morphology and evolution of the flare. In § 3, we investigate the flare kernel motion using high-cadence and high-resolution Hα observations, from which we can infer, in § 4, the temporal variation of the electric field in the RCS. In § 5 we analyze hard X-ray and microwave bursts in comparison with the RCS electric field. Section 6 is dedicated to discussions, and our conclusions are presented in § 7.

2. OVERVIEW

In this paper, we present ground-based and satellite observations of a C9.0 flare which occurred in NOAA 8906 (S16°, W31°) on 2000 March 16. A detailed description of the instruments and data reduction was given in an earlier paper by Qiu et al. (2001). The high-cadence (0.1 s) and high-resolution (0.″36 pixel^{-1}) BBSO H$\alpha-1.3$ Å images, combined with the *Yohkoh* hard X-ray and OVSA microwave observations, are the critical data sets for our study. Apart from providing the time profiles and spectral information, the X-ray and microwave observing instruments have multichannel imaging capability. Hard X-ray images at *Yohkoh* Hard X-Ray Telescope (HXT) L, M1, and M2 channels (14–23–33–53 keV) are obtained using the maximum entropy method (Sakao 1994; Sato, Kosugi, & Makishima 1999), the image FWHM being typically 5″–10″. The microwave observations were taken at 40 frequencies from 1 to 18 GHz with a 10 s time cadence. For radio imaging, we use a standard CLEAN method (Högbom 1974), combined with self-calibration (Cornwell & Fomalont 1999), both of which are included in the solar microwave imaging software of the OVSA. The radio images shown in the paper are obtained by combining the OVSA data at three frequencies, 9.0, 9.4, and 10 GHz. The antenna configuration at the time of imaging gives an elongated CLEAN beam with a FWHM of 5.″9 × 17″. We also collect soft X-ray data from *Yohkoh* and magnetograms from

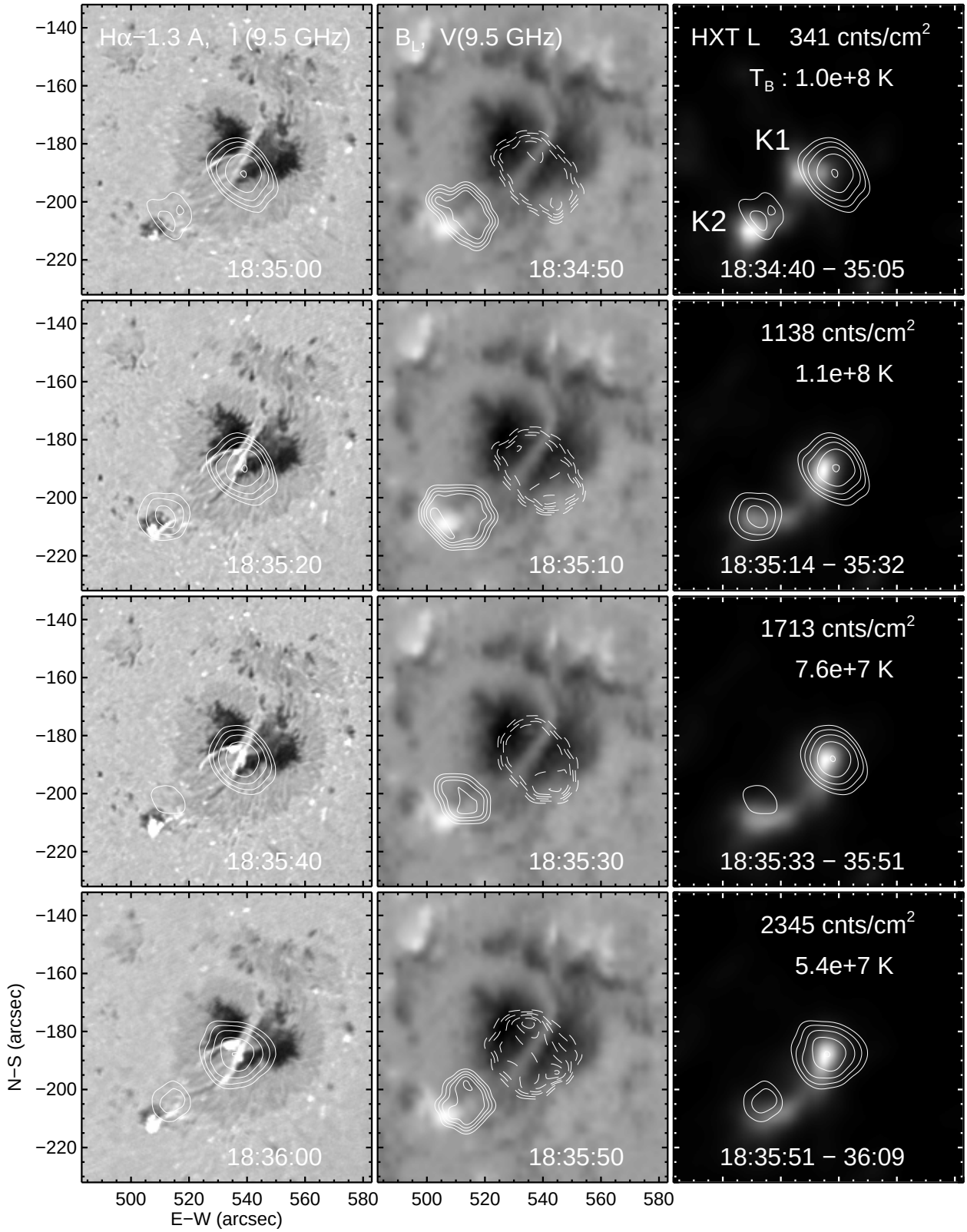

FIG. 1.—Evolution of the flare. *Left*: BBSO Hα − 1.3 Å images with contours of the OVSA microwave intensity map at 9.5 GHz, the contour levels being 0.30, 0.40, 0.54, and 0.73 of the maximum intensity. *Middle*: BBSO longitudinal magnetogram at 18:27 UT with contours of the microwave polarization map. The solid lines denote the right circular polarization and the dashed lines left circular polarization, the contour levels being 0.1, 0.2, 0.3, 0.4, 0.5, 0.6, 0.7, 0.8, and 0.9. *Right*: Hard X-ray images from *Yohkoh* HXT L channel with contours of the microwave intensity map at 9.5 GHz (same as in the left panel). Indicated are the maximum X-ray counts for each integration period and the bright temperature of each radio map.

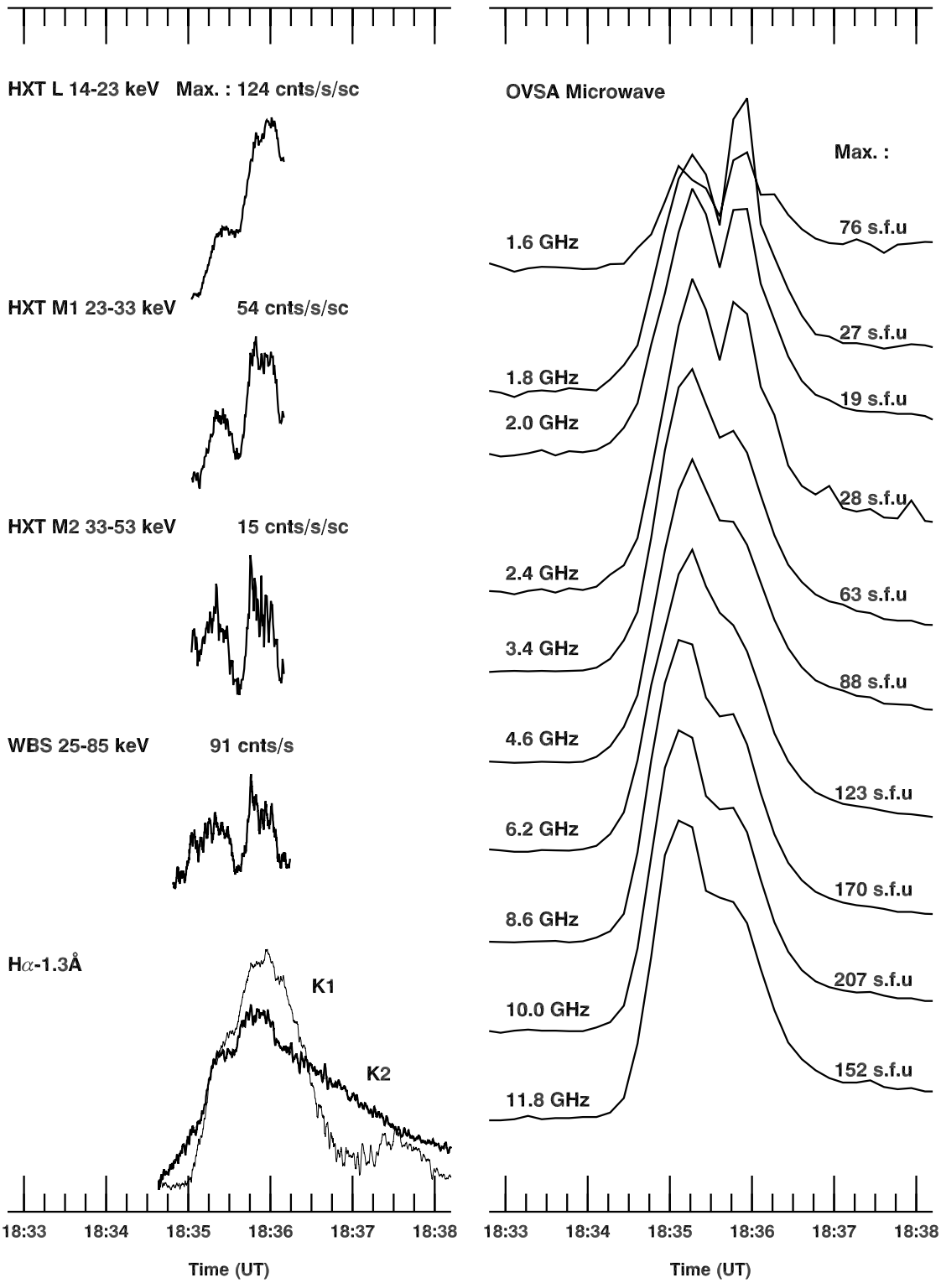

FIG. 2.—Hα − 1.3 Å, hard X-ray, and microwave time profiles of the flare. Hα light curve shows the integrated intensity over each flare kernel with the preflare background subtracted. The maximum X-ray counts rate at each channel and the maximum microwave flux at each frequency are indicated.

BBSO and the Michelson Doppler Imager (MDI) in order to understand the general configuration of the flare.

Figure 1 shows the morphological evolution of the flare observed by various instruments and the co-aligned magnetogram of the active region obtained at BBSO at 18:27 UT. Throughout the impulsive phase, at all wavelengths, we can distinguish two bright flare kernels, designated as K1 and K2 in this paper. Within the image resolutions of the *Yohkoh* and OVSA instruments, the two flare kernels observed at hard X-ray and radio wavelengths can be regarded as coincident with the Hα kernels. K1 is located at a light bridge splitting a sunspot of negative polarity into two halves, and K2 is located in a pore of positive polarity. The radio polarization maps (see the middle column in Fig.

1) further show that the emission source in K1 and that in K2 have opposite polarization components because of the opposite magnetic polarities. The radio flux in K1 is much stronger than in K2, probably due to the stronger magnetic fields at K1.

In Figure 2, we plot the time profiles of the flare. Integrated intensity of the Hα emission, with the preflare background subtracted, is derived from the spatially resolved sources K1 and K2. Hard X-ray light curves are provided by the *Yohkoh* HXT and Wide Band Spectrometer (WBS) pulse count detector in the energy range of 25–85 keV. The *Yohkoh* hard X-ray observations cover only the impulsive phase, followed by a long data gap during the decaying phase. Light curves of radio emission at various frequencies are also presented that have a time cadence of 10 s. At all wavelengths, the impulsive phase light curves exhibit two major peaks. The similarity in the flare morphology and time profiles at Hα, hard X-ray, and radio wavelengths suggests that a common energy release process produces emission at the three wavelengths; it is therefore appropriate to compare observations at these wavelengths to gain an understanding of the energy release process in this event.

In order to understand the magnetic configuration of the flare, we also examine the connectivity between the two flare kernels by computing the temporal correlation in the light curves between K1 and K2. The cross-correlation between the two Hα curves, with zero lag, is larger than 90%, indicating a simultaneity in the flare emission at the two kernels. The spatially resolved hard X-ray image sequence shows that the two kernels also have temporally correlated hard X-ray light curves and the same energy spectrum to within the HXT spectral resolution. These facts suggest that the two kernels are connected by magnetic field lines along which accelerated electrons, as a result of the coronal magnetic reconnection, precipitate simultaneously at the two kernels in the lower chromosphere. The two kernels are therefore regarded as the conjugate footpoints of a flare loop.

3. Hα KERNEL MOTION

A more careful look at the time sequence of the high resolution Hα − 1.3 Å images suggests that, according to the morphological evolution, the flare kernels K1 and K2 can each be further resolved into two parts, namely, K1a and K1b, and K2a and K2b, as shown in Figure 3. K1a and K1b are both elongated structures separated by the light bridge, while K2a and K2b are confined patches, K2a being located in the stronger magnetic field region relative to K2b. The subsequent analysis is therefore conducted for the four patches separately.

The high-cadence Hα movie further reveals that the location of the brightest emission inside the flare kernels evolves with time. Presumably, at a given time, the site of the brightest emission is where the instantaneous energy deposition occurs, since the timescale of the chromospheric response to the precipitation of nonthermal electrons is very short (Canfield & Gayley 1987; Gayley & Canfield 1991). Such a presumption is also supported by the observation that the Hα − 1.3 Å maximum intensity light curves bear more similarities to ≥20 keV hard X-ray light curves, i.e., the maximum light curves exhibit a faster rise and decay, and better reveal fine temporal structures on timescales of a few seconds, than do the integrated intensity light curves (Fig. 3).

To follow the locality of the flare energy release at the footpoints, in Figure 4 we mark the trajectories of the brightest pixels in K1a, K1b, K2a, and K2b, respectively, with the changing color tones indicating the time lapse. The contours of the longitudinal magnetogram obtained by MDI at 18:27 UT are superposed to indicate the magnetic field along the trajectories. The figure shows significant motion of bright centers in K1a and K1b. As we can confirm from the movie, such a motion is not due to seeing effects or a misalignment. No significant motion is seen in K2, probably because the magnetic field lines at K2 are converging into a small area which cannot be further resolved, as also suggested by Qiu et al. (2001). Note that although the term "motion" or "moving" is frequently used throughout this paper, what is observed as the shift of the emission sources is not a real motion of the magnetic field lines at the lower atmosphere, but rather the changing locations of the excitation in the chromosphere. In the context of magnetic energy release via magnetic reconnection, the instantaneous energy deposition reaches the chromosphere from the corona along the newly reconnected magnetic field lines, so such a motion depicts the precipitation of electrons along adjacent magnetic field lines, which are successively reconnected as the magnetic energy release proceeds in the corona.

Figure 4 reveals several properties in the kernel motion in K1a and K1b. Most importantly, the average motion along K1a and K1b follows a systematic and regular pattern, according to which we can relate the footpoint motion to the progressive magnetic reconnection in the corona. Apart from this similarity to many dynamic two-ribbon flares, other respects of the motion are quite different from a two-ribbon flare. First, there is not a well-defined "ribbon" aligned in a direction perpendicular to the motion vector, indicating that there is not an arcade structure in this event. Second, brightenings at the two kernels do not resemble the most typical case of a two-ribbon flare, in which the two ribbons residing in opposite magnetic polarities move apart from each other and away from the magnetic inversion line. Instead, brightenings in K1 are moving more or less toward K2, while K2 remains motionless. Such a moving pattern and the asymmetry in the motion between the two kernels represents a peculiar magnetic field geometry in the corona, which is different from the stereotypical Kopp-Pneuman coronal configuration (Kopp & Pneuman 1976; also see Forbes & Acton 1996). We also note that the brightenings in K1a and K1b start close to, but on either side of, the light bridge and then move away from it. In other words, both the brightening and the motion in K1 are spatially divided by the light bridge. Particularly, the average trajectory of the brightest emission center in K1a suggests a unidirectional motion proceeding nearly along a straight line and into stronger magnetic fields. On the other hand, the motion in K1b, although also following nearly a straight line, is not unidirectional; the brightest center sometimes moves back and forth, and the motion is almost parallel to the isogauss contours aligned with the outer edge of the light bridge. These facts suggest that the driving of the motion, and possibly the inferred magnetic field organization in the active region, is asymmetric about the light bridge.

Since the morphology and motion pattern in this event largely differ from a typical two-ribbon flare, it suggests a peculiar magnetic configuration. One possible scenario is

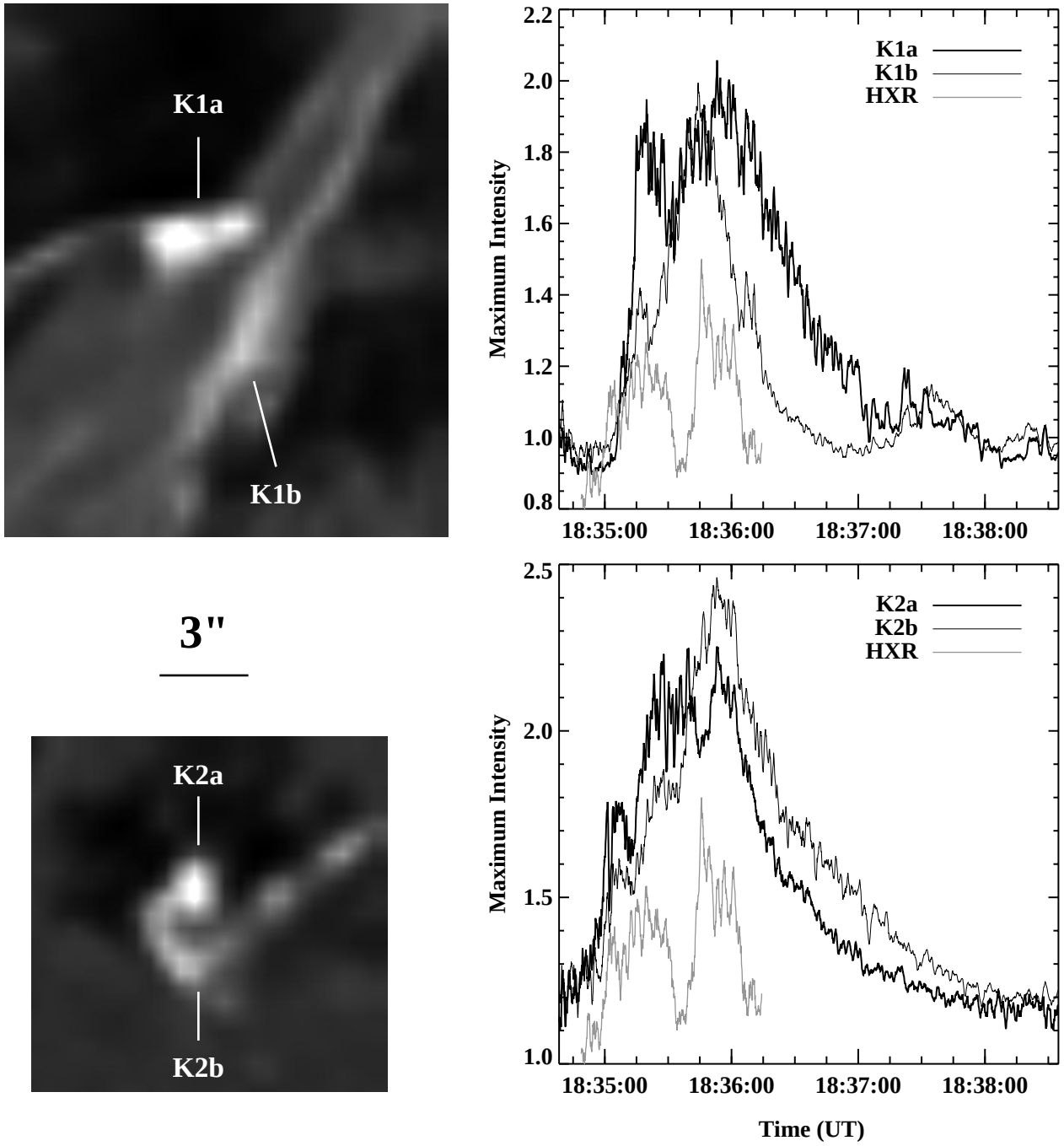

FIG. 3.—*Left*: Magnified subframe images of the Hα flare kernels at 18:35:20 UT, showing the spatially resolved fine structures within each kernel. *Right*: The spatially resolved Hα maximum intensity light curves at each kernel, superposed with the hard X-ray light curve from *Yohkoh* WBS. The X-ray light curve is arbitrarily normalized.

shown schematically in Figure 9. The magnetic field lines rooted at K1a/K1b away from the light bridge are connected to those rooted at K2a/K2b at progressively greater heights. As the reconnection goes on and the reconnection point moves up, more open field lines become closed, and the separatrix dividing the two flux regimes moves out along K1a/K1b. As a result, the footpoint brightening spreads outward as observed. This case is a two-dimensional resemblance to a two-ribbon flare, if we ignore the translational dimension in this particular event.

4. INFERRED ELECTRIC FIELD IN THE RCS

The systematic motion of flare kernels sweeping through the magnetic field lines offers a measure of how fast the magnetic flux is convected into the diffusion region where the reconnecting current sheet is formed. In a two-dimensional configuration, equation (3) can be used to determine the evolution of the electric field $E_c(t)$ by measuring the instantaneous velocity $V_{\|}(t)$ and the magnetic field B_n. Note that for a two-ribbon flare whose two ribbons consist of footpoints of an arcade of magnetic loops, this simplified relation contains an assumption of a translational symmetry in the coronal field configuration, so $E_c(t)$ is uniform along the current sheet that runs along the translational dimension and connects two null points (Forbes & Lin 2000). Therefore, $E_c(t)$, on the one hand, is by itself a

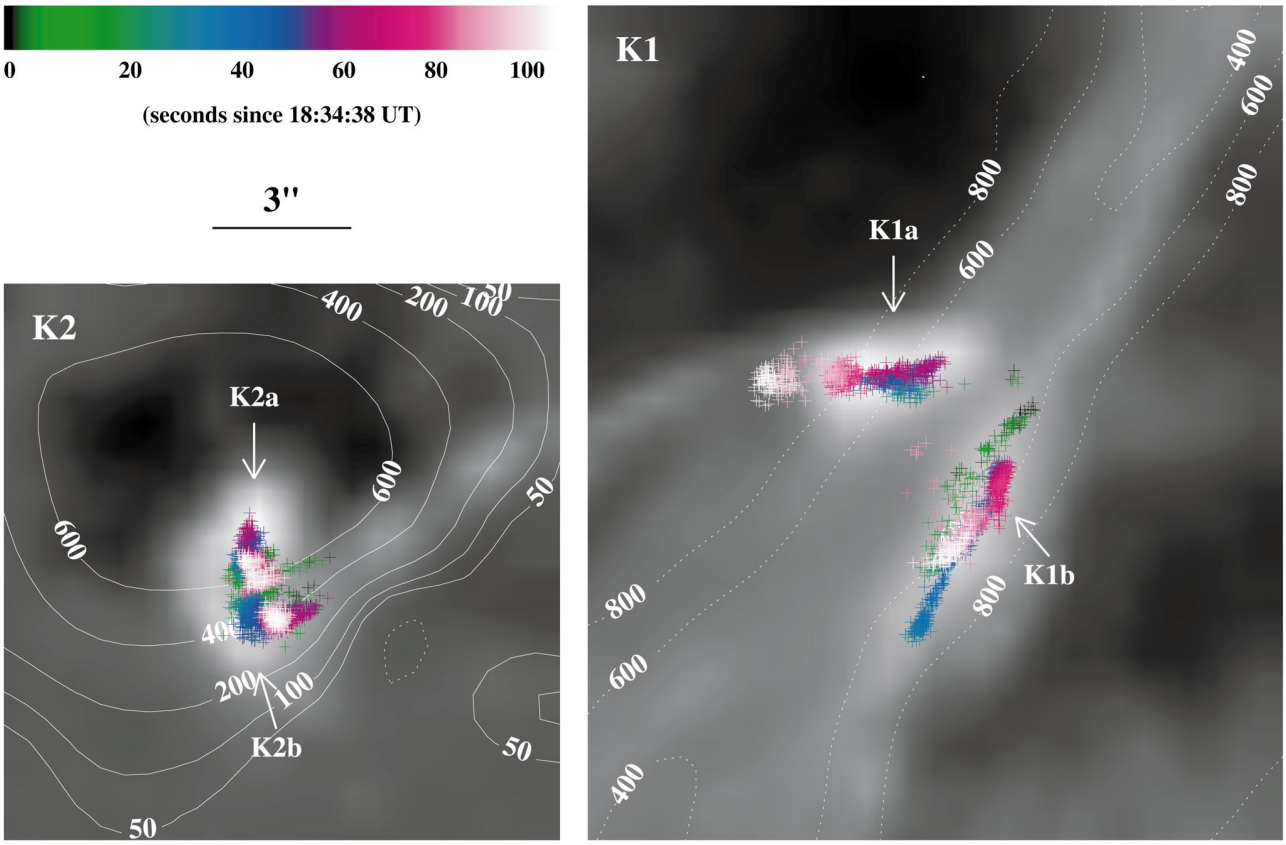

FIG. 4.—Trajectories of the brightest pixels in flare kernels K2 (*left*) and K1 (*right*). The time lapse is marked by the color table. The solid (dotted) contours indicate the positive (negative) longitudinal magnetic field obtained by MDI at 18:27 UT, the contour levels being given in units of gauss.

measure of the local reconnection rate and, on the other hand, when multiplied by the length of the current sheet, also represents a measure of the global reconnection rate as the voltage drop along the length of the current sheet.

Although the event studied in this paper is not a two-ribbon flare, we can still adopt a two-dimensional approach, i.e., equation (3), to derive the electric field, because the dimension perpendicular to the motion is much smaller than the dimension along the motion, and the systematic motion we can detect is an average along the cross section perpendicular to the motion direction. In this case, it is sufficient to assume the uniformity of the electric field along the cross section, with an average field strength derived from the average motion of the kernel. Particularly, for the ensuing investigation of X-ray-and microwave-emitting electrons, the electric field strength, rather than the voltage drop along the RCS, is a more important physical parameter. This point will be discussed in § 6.

In view of the apparently bifurcated motion between K1a and K1b (§ 3), we measure the kernel motion velocity $V_{\|}(t)$ in these two patches separately. Since there is not a resolvable systematic motion in either K2a or K2b, we do not measure the velocity in these two patches. In the following, we present, in Figures 5 and 6, the measurement of the motion velocity, magnetic field, and inferred electric field from K1a and K1b, respectively.

Figure 5*a* shows the time variation of the displacement of the brightest Hα emission in K1a with respect to the starting position averaged around 18:35:00 UT. The overplotted thick solid line is a 10 s running mean of the displacement curve, and the thick dashed line is a least-squares fit to a straight line. The time derivative of these curves gives the velocity of the kernel motion as shown in Figure 5*b*. The 10 s smoothed curve yields a nonconstant speed whose maximum is about 100 km s^{-1}, and the straight-line fit gives a constant speed of 20 km s^{-1}. These values are in the same order of magnitude as the results reported in earlier observations (Kitahara & Kurokawa 1990; Falchi et al. 1997), yet our measurement is more accurate owing to the high cadence and resolution of the current observations.

For the measurement of B_n, since the active region is not far from the solar disk center, the observed longitudinal magnetic field $B_{\|}$ can be used as B_n. Figure 5*c* shows the variation of B_n, i.e., the magnetic flux density traversed by the footpoint motion with time. The brightening in K1a starts in a region of relatively weak fields of about 500 G and moves into stronger fields of up to 900 G. To make Figure 5*c*, we use only a single magnetogram taken by MDI before the flare, because the longitudinal magnetic field does not change significantly during the short lifetime of the flare. Plots similar to Figure 5*c* can be made using magnetograms taken at BBSO at different times, and the general trend in these plots is the same as shown by using the MDI magnetogram. Note that the plot in Figure 5*c* resembles well that in Figure 5*a*, suggesting that the motion along K1a is inclined to the magnetic gradient by a fixed angle.

Figure 5*d* shows the temporal evolution of the electric field $E_c(t)$ as derived from Figures 5*b* and 5*c* using equation (3). The maximum electric field inferred from the motion in K1a is about 90 V cm^{-1}, more than an order of magnitude greater than the previously reported value of 2 V cm^{-1} by

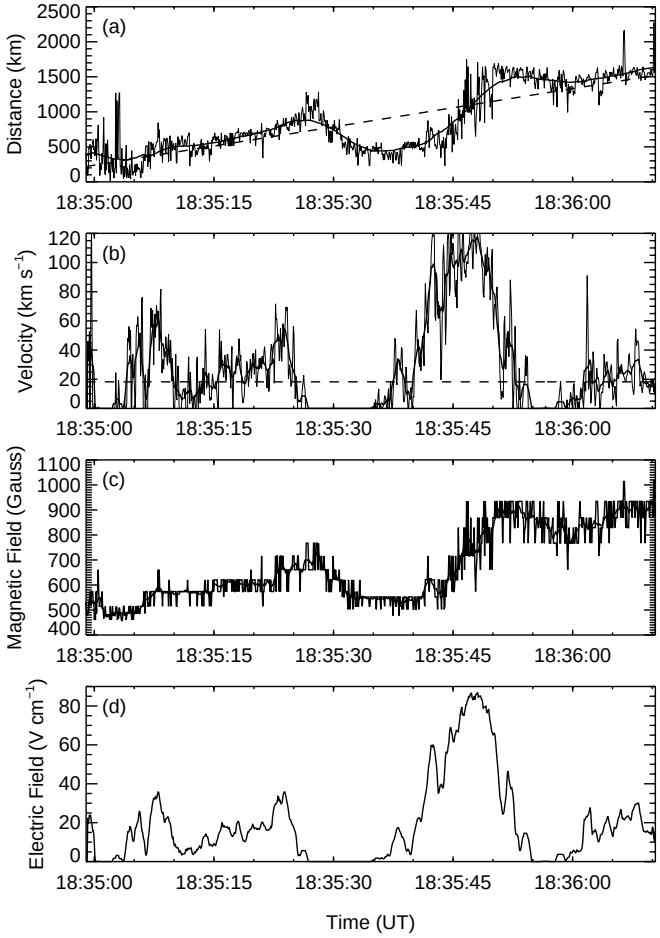

FIG. 5.—Electric field inferred from kernel motion in K1a. (*a*) Time variation of the kernel displacement since 18:35:00 UT. The smooth solid line shows the 10 s running mean of the curve, and the dashed line is the least-squares fit of the curve to a straight line. (*b*) The motion velocity derived from (*a*). The solid line indicates the nonconstant velocity from the 10 s smoothed curve, and the dashed line indicates the constant velocity from the straight-line fit. (*c*) The longitudinal magnetic field traversed by the motion. (*d*) The inferred electric field variation using the nonconstant velocity (see text).

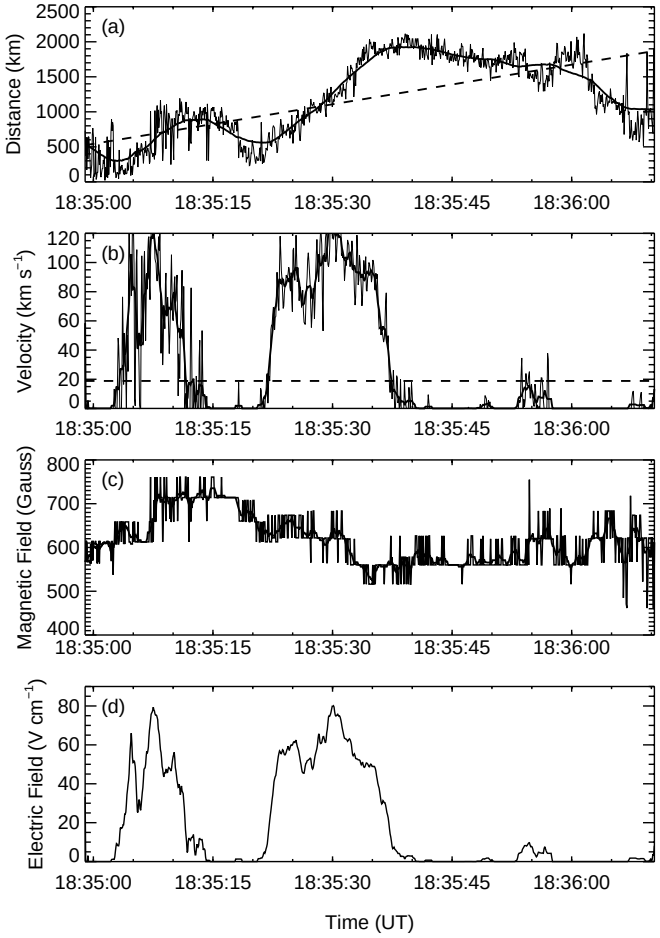

FIG. 6.—Same as Fig. 5 but for K1b

Poletto & Kopp (1986). This value is also greater, by a factor of 2–3, than the measurements based on Stark effect by Foukal & Behr (1995), who reported a field ≈ 35 V cm^{-1}. Such a large value is partly due to the fact that we measure more accurately the instantaneous velocity rather than using a smaller average velocity, and also that the flare kernel K1a is moving into the sunspot umbra, where the magnetic fields are strong. Despite the large inferred electric field, the flare is confined to a small volume so that the overall energy released is not large.

In Figure 6, we make similar plots for K1b. From the 10 s smoothed displacement curve in Figure 6*a*, we obtain the velocity $V_{\|}$ changing between 20 and 100 km s^{-1} during the impulsive phase (Fig. 6*b*). Note that in contrast to K1a, the motion in K1b is almost along the isogauss contour of the magnetic field at the level of about 600 G (Fig. 6*c*). The electric field $E_c(t)$ inferred from K1b is illustrated in Figure 6*d*, the maximum field strength being comparable with that from K1a.

We sum the electric field strength inferred from the motions in K1a and K1b to give the overall electric field in the RCS during the flare impulsive phase. This is plotted

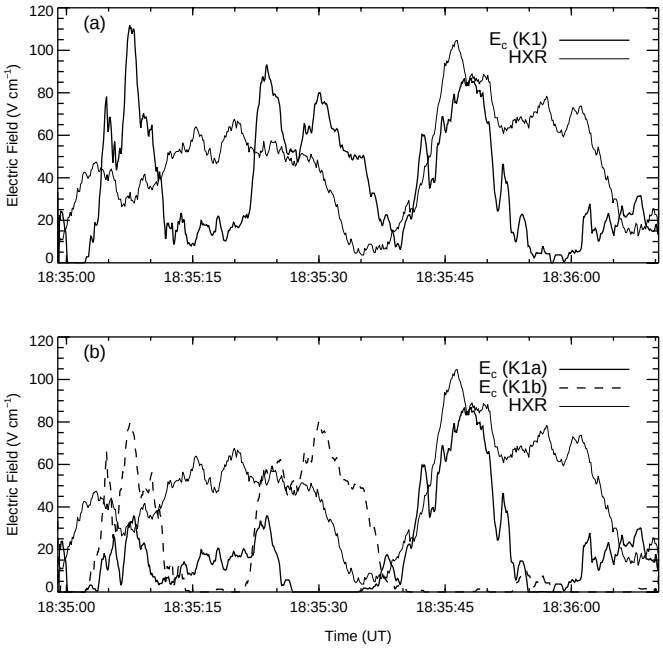

FIG. 7.—(*a*) The overall electric field (*thick solid line*) summed from K1a and K1b in comparison with the hard X-ray 25–85 keV light curve (*thin solid line*) from *Yohkoh* WBS. (*b*) The electric fields from K1a (*thick solid line*) and K1b (*thick dashed line*), respectively, in comparison with the hard X-ray emission (*thin solid line*). The hard X-ray light curve is arbitrarily normalized.

with the thick solid line in Figure 7*a*. The time profile of the electric field offers a direct indication of the variation of the magnetic reconnection rate, which we compare with the hard X-ray light curve shown by the thin solid line in Figure 7*a*. There is a certain temporal correlation between the two curves, $E_c(t)$ and hard X-ray, especially during the sharp rise of the second, also the major, emission peak. Such a fact indicates that at least during the major impulsive phase from 18:35:40 to 18:35:50 UT, the footpoint kernel motion can trace well the progressive magnetic reconnection in the corona, and furthermore, the hard X-ray flux, presumably due to nonthermal electrons accelerated during the reconnection, varies with time in the same way as the electric field strength inside the RCS. At about the hard X-ray maximum, the electric field also reaches a maximum of 90 V cm^{-1}.

We should emphasize that the good correlation between hard X-rays and the electric field is found only during a limited time, the impulsive rise of the second peak from 18:35:40 to 18:35:50 UT and is determined only by the motion in K1a, while the correlation is poor at other kernels and other times. This result may only provide a partial support of the discussed theoretical model, which relates the generation of the RCS in the corona to the footpoint kernel motion. It is however likely that the specific magnetic field configuration in this event limits the applicability of the reconnection theory (Forbes & Priest 1984) to some part of the flare. First, we notice that the good correlation is due to the large acceleration in the spread of brightenings along K1a at the time of the rapid rise in X-ray emission (Fig. 7*a*), which is in agreement with the theoretical predictions. On the other hand, the poor correlation at early times (before 18:35:30 UT) may be due to the fact that the motion in this period is not so regular as to be described by a systematic pattern. Second, K1a and K1b exhibit quite different patterns of motion, in that the motion in K1a is toward stronger magnetic fields whereas K1b is principally moving along the isogauss magnetic field region (Fig. 4). This gives rise to different types of time profiles of the electric fields inferred from K1a and K1b, the former being partially correlated with the X-ray emission and the latter bearing no resemblance to X-rays. Such bifurcation may represent the different structures and processes of the coronal reconnection at different locations, all of which do not conform to the configuration of magnetic reconnection postulated by Forbes & Priest (1984). Finally, we note that whether there exists a correlation between $E_c(t)$ and X-rays also depends on how X-ray–emitting electrons are produced in the RCS. The fact that a correlation is seen only for a certain episode may indicate the existence of different electron acceleration mechanisms during different episodes of the flare. Clues to the acceleration mechanism are provided by the energy and frequency dependence of hard X-rays and microwaves, respectively, as will be further discussed in the next section.

5. COMPARISON OF X-RAY AND MICROWAVE ELECTRONS

By relating the Hα flare kernel motion to the progressive magnetic reconnection in the corona, we have derived the macroscopic electric field inside the RCS as $\sim$90 V cm^{-1} at the maximum. This electric field is far greater than the local Dreicer field (Dreicer 1959) in the corona, which is at the level of $\sim 10^{-5}$ V cm^{-1} (Holman 1985). A direct consequence of having such a super-Dreicer field is the simultaneous acceleration of almost the whole electron population out of their original thermal Maxwellian distribution. With the DC field acceleration mechanism, the maximum energy that electrons can achieve basically depends on the electric field strength and the distance traversed by the electrons along the field. It is, however, believed that the maximum energy corresponding to the voltage drop along the whole length of the RCS cannot be realized because of either hyperfilamentation of the current sheet (Holman 1985) or the drift of electrons in the presence of the magnetic field transverse to the electric field (Litvinenko 1996). Both authors suggest that the maximum energy that electrons can achieve via the DC acceleration mechanism would be $\leq$100 keV, which largely depends on the parameters postulated in their models. We may give an empirical point of view that, in this event, the DC acceleration be a major acceleration mechanism for X-ray–producing electrons, as evidenced by the close resemblance between the electric field evolution and the time profiles of hard X-rays up to $\sim$85 keV, at least during a portion of the impulsive phase.

The same population of electrons with somewhat different energy can emit microwaves (e.g., Nitta & Kosugi 1986; Kosugi, Dennis, & Kai 1988), and we further investigate whether the time profiles of microwaves correlate with the inferred electric field. As shown in Figure 2, there is a temporal correlation between low-frequency radio bursts and X-ray emission to the extent that both exhibit two peaks and a dip in between during the impulsive phase. However, the correlation becomes less clear at high frequencies, where the first peak dominates, and the dip and the second peak are less distinct. Since microwave emission at optically thin frequencies ($\geq$10 GHz in this event) is more sensitive to the variation of high-energy electrons, we consider that the temporal behavior of the microwave-emitting electrons would differ from that of the hard X-ray electrons. Because of the sensitivity of microwaves to the magnetic field, one may consider that the radio time profile may be due to temporal variations of the magnetic field rather than variations of electrons. However, based on Figures 1 and 5, we find it unlikely that the change of the magnetic field with time would result in the observed temporal behavior of the microwaves. It is more likely that there are, in this event, effectively two different populations of electrons: one gives rise to the low-energy hard X-ray emission observed by HXT (14–53 keV) and WBS ($\leq$85 keV), and the other consists of several hundred keV electrons emitting microwaves.

In order to check the hypothesis that microwaves and hard X-rays in this event are produced by electrons at different energy ranges, we compare the spectrum and number of electrons inferred from the hard X-ray emission with those from the microwave emission, under the assumption that each electron population has a single power-law distribution in the form of $\sim E^{-\delta}$. Figures 8*a*–8*d* show the brightness temperature spectra at four time intervals. The brightness temperatures are determined from the observed total power spectrum along with the source diameter ($\sim$20″) estimated from the radio image (Fig. 1). The nearly flat part at the low frequencies is the optically thick regime giving the effective temperature of the electrons, and the decreasing part of the spectrum at high frequencies is the optically thin regime of which the spectral index, Γ, is directly related to the electron power-law index by $\delta = (\Gamma - 0.78)/0.9$ (Dulk & Marsh 1982). The fit to determine the spectral index, Γ, is shown with the guidelines in

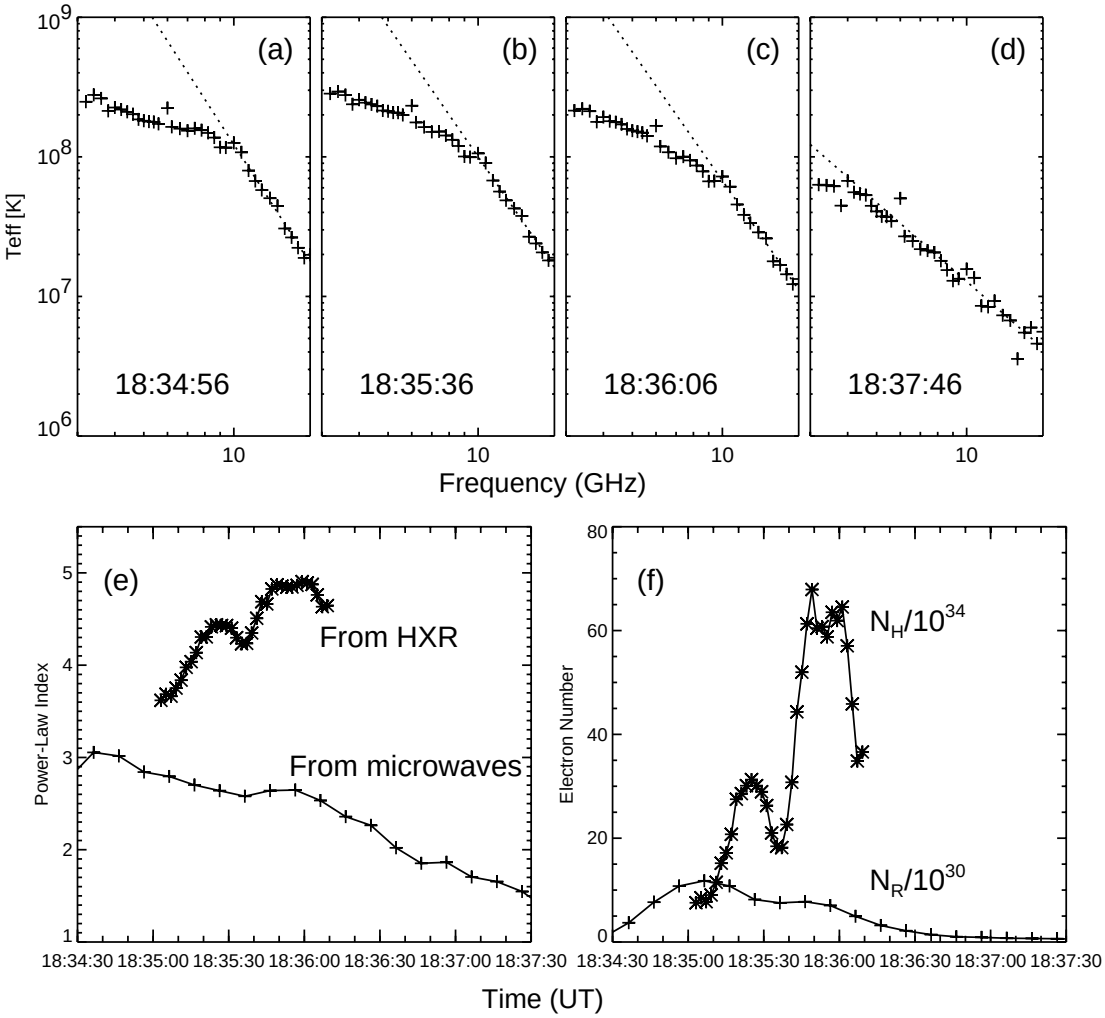

FIG. 8.—(*a*)–(*d*) Microwave brightness spectra at four time intervals. The dotted lines are to guide the spectral fit to the optically thin part. (*e*) Time variations of the hard X-ray and microwave electron power indices. (*f*) Time variations of numbers of electrons emitting X-ray and ≥ 10 GHz microwaves.

the figures. We measure $\Gamma = 2.2$–4.0, which gives $\delta \approx 1.5$–3 for the microwave-emitting electrons. We also determine the power-law index of hard X-ray spectrum from the average ratio between hard X-ray counts in HXT M1, M2, and H channels, which gives $\gamma \approx 2.5$–4. Under the assumption that the hard X-rays are due to thick-target emission, we use the relation $\delta = \gamma + 1$ (Brown 1971), which yields $\delta \approx 3.5$–5 for the X-ray emission electrons. Figure 8*e* illustrates the comparison of the electron power-law indices derived from the microwaves and the hard X-rays, respectively. The microwave electrons have a much harder spectrum than the ≤ 100 keV hard X-ray electrons. The result that the microwave spectrum indicates the presence of harder electrons than X-ray electrons has been obtained in other events as well. It is interpreted as due to the fact that the higher energy part of the electron distribution contributes to microwave emission (e.g., Silva, Wang, & Gary 2000). We consider that the same interpretation would apply to this event as well.

We also compare the numbers of electrons emitting X-rays and microwaves, respectively. For X-rays, the count rates recorded in HXT M1, M2, and H channels are calibrated (Sato et al. 1998) and integrated to yield the X-ray photon rates $I(\epsilon_0)$ at an assumed cutoff energy $\epsilon_0 = 20$ keV. Based on the thick-target bremsstrahlung model (Brown 1971; Lin & Hudson 1976), with $I(\epsilon_0)$ and γ, we can derive the number of hard X-ray power-law electrons per second $N_H = \int_{E_0}^{\infty} F(E)dE$, where $F(E)$ is determined by

$$F(E) = 4.21 \times 10^{33}\gamma(\gamma - 1)^2 B[\gamma - \tfrac{1}{2}, \tfrac{1}{2}]AE^{-\gamma-1}, \quad (4)$$

and A is derived from $I(\epsilon_0) = \int_{\epsilon_0}^{\infty} A\epsilon^{-\gamma}d\epsilon = A(\gamma - 1)^{-1}\epsilon_0^{-\gamma+1}$. The electron energy cutoff E_0 is taken as 20 keV. For microwaves, we first calculate the theoretical emissivity η_ν at an optically thin frequency ν using the simplified expressions given by Dulk & Marsh (1982):

$$\frac{\eta_\nu}{N} \approx 3.3 \times 10^{-24}10^{-0.52\delta} \times B(\sin\theta)^{-0.43+0.65\delta}\left(\frac{\nu}{\nu_B}\right)^{1.22-0.90\delta}, \quad (5)$$

where N is the number of electrons per cm^3 integrated over $E \geq 10$ keV. We use the electron power-law index δ derived from Γ (Fig. 8*e*), and assume that the magnetic field is $B = 700$ G and the viewing angle of the magnetic field is $\theta = 45°$, so as to determine the emissivity per electron, η_ν/N. The ratio of the observed flux at the frequency ν to η_ν/N gives the number of electrons N. The assumed power-law distribution is written as $n(E) = (\delta - 1)(N/E_0)(E/E_0)^{-\delta}$,

from which, we can determine the number of electrons with energy above 100 keV as $N_R = \int_{100\,\mathrm{keV}}^{\infty} n(E)dE$. Figure 8*f* shows the time profiles of N_H and N_R. It is seen that during the early impulsive phase, N_R starts to rise earlier and reaches the maximum ahead of N_H by about 20 ± 10 s, hence there is not a good temporal correlation between N_H and N_R.

From the above analyses which show the very different temporal behaviors and energy spectra between microwaves and hard X-rays, it is reasonable to presume that high-energy electrons ($\geq$100 keV) responsible for the radio emission are not an extension of the low-energy electrons ($\leq$100 keV) in the same power-law spectrum. Specifically in this event, the low-energy electrons are produced as a direct response to the electric field in the RCS via the DC field acceleration, while another acceleration mechanism also exists to generate high-energy electrons emitting microwave bursts. Identifying this additional acceleration mechanism with a specific process is beyond the scope of the present paper, and we comment on only two points of these different acceleration processes. First, the existence of a correlation between the electric field and $\leq$100 keV X-rays indicates that the maximum energy that electrons attain via the DC field acceleration appears to be about 100 keV. This is in agreement with theoretical predictions (Litvinenko 1996). Second, in view of the multifrequency microwave time profiles (Figs. 2 and 8), we can suggest that the other unknown acceleration mechanism is probably switched on during the rise of the first hard X-ray peak (Fig. 8), and soon diminishes or stops before the second X-ray emission peak, so the high-frequency radio emission gradually decays after its first peak.

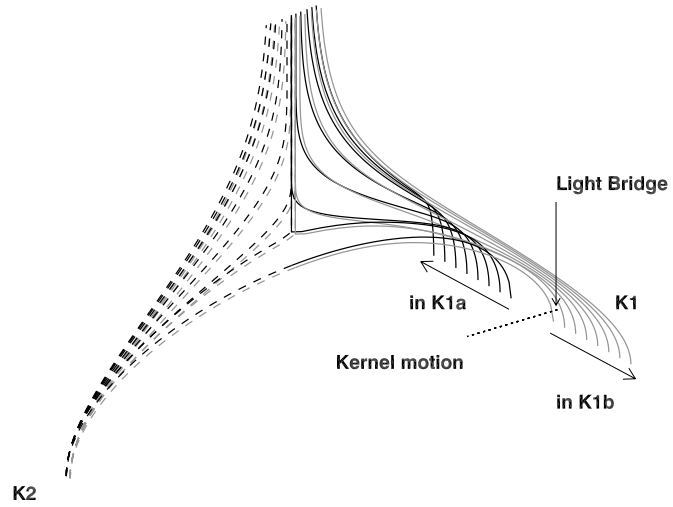

FIG. 9.—Cusp structure. Schematic illustration of the possible magnetic configuration of the flare showing magnetic reconnection of open field lines.

6. DISCUSSION

6.1. *Where Is the Reconnection Point?*

By invoking the progressive magnetic reconnection model (Forbes & Lin 2000 and references therein) to interpret the systematic Hα footpoint kernel motion, we can derive evolution of the macroscopic electric field inside the RCS which are believed to form at the separator point (two-dimensional) or along a separator line (three-dimensional). For the event studied, Figure 9 suggests a possible magnetic configuration which is nearly a Kopp-Pneuman type open field line configuration. In such a scenario, the separator is well defined at the point where a pair of antiparallel field lines meet and reconnect to form a closed field line, and the front of the chromospheric brightening marks the instantaneous location of the chromospheric intersection of the separatrix dividing the open field line domain and closed field line domain.

A difficulty with such a scenario is that, in this flare, no cusplike structure is visible in the soft X-ray observations, while such a structure would be expected for the configuration illustrated in Figure 9. It is possible that since the active region is not far from the solar disk center, if the flare loop is not much inclined to the photospheric plane, the cusp may not be as easily discernible as in a limb flare, or the cusp region may exist but not appear bright in soft X-rays. Still, we cannot exclude the possibility that the cusp structure does not exist. Nevertheless, as mentioned in § 1, the validity of using equations (1)–(3) to relate the chromospheric signature to the coronal magnetic reconnection is not confined to only the Kopp-Pneuman configuration; instead, it needs two prerequisites, independent of the detailed field configuration: (1) the chromospheric brightenings well trace the locations of the separatrices, and (2) the moving brightenings correspond to a set of magnetic field lines which successively reconnect in an organized manner rather than randomly. In these circumstances, the measured kernel motion velocity is physically meaningful. For the second point, we regard that the progressive magnetic reconnection is indeed occurring during the impulsive phase because of the systematic nature of the kernel motion observed in this flare. For the first point, an increasing number of observations have identified that chromospheric emission is by and large located at or along the chromospheric intersection of separatrices (Demoulin et al. 1994; Mandrini et al. 1993, 1995), or quasi-separatrix layers (Demoulin et al. 1996, 1997), disregarding the detailed magnetic configuration. So, existence of a preflare open field line configuration and the resultant cusplike structure after the reconnection are not a necessary condition in order to justify the usage of equations (1)–(3), as long as the preflare field lines rooted from K1 and K2 are organized in such a way that enables a progressive manner of magnetic reconnection.

6.2. *Prospect of Fragmented DC Acceleration*

Though the model of the progressive magnetic reconnection and the consequent energy release is well adopted for the type of dynamic solar flares, the MHD approach of the model cannot address the issue of how the released magnetic energy is converted to heating the plasma and accelerating charged particles. Nevertheless, our observational results offer a nice clue that in this event, at least during a certain phase of the flare, the DC electric field plays an important role. Given the maximum electric field strength $E_c \approx 90$ V cm^{-1}, to accelerate electrons to up to 100 keV as revealed by X-ray observations, the required effective acceleration length is $\Delta l \leq 10$ m. If we take that the length of the flare kernel cross section, which is perpendicular to the motion direction, is approximately the full length of the current sheet l, we find $l \approx 2'' \approx 10^3$ km, so that

$\Delta l/l \approx 10^{-5}$. So, electrons are not accelerated in a single beam running through the full length of the RCS. This avoids the difficulty in the single-beam model that would give rise to an unphysically huge magnetic field induced by the current (Holman 1985; Litvinenko 1996).

In his flux pile-up model, Litvinenko (1996) introduced a finite longitudinal magnetic field $B_{\|}$ along the electric current together with a transverse magnetic field component $B_{\perp}$ in the reconnection region. The action of the transverse field upon accelerated particles helps electrons escape quickly from the RCS, so that the actual acceleration length can be a few orders of magnitude smaller than the full length of the RCS. In this event, at the flare maximum, $\Delta l/l \approx 10^{-5}$. Since this quantity is crucially decided by the ratio of $B_{\|}/B_{\perp}$, our result confirms that in this event, $B_{\perp}$ at the reconnection region is nontrivial with respect to $B_{\|}$. According to Litvinenko (1996), the estimated electron number per second is $N = 4bln_0(cE_c/B_0)$, where the current induced magnetic field is $B_0 = (4\pi eE_c n_0 \Delta l)^{1/2}$. Given the RCS half-width $b \approx l \approx 10^8$ cm and the electron density outside the sheet $n_0 \approx 10^{10}$ cm^{-3}, we get $N \approx 3 \times 10^{36}$ s^{-1} at the flare maximum, which is of the same order of magnitude as the value derived from X-ray observations shown in Figure 8.

7. CONCLUSIONS

In the present paper, we employ high-cadence and high-resolution H$\alpha-1.3$ Å observations of a C9.0 flare obtained by BBSO to study the chromospheric signature of coronal magnetic energy release during the impulsive phase. In the context of the progressive coronal magnetic reconnection (Forbes & Lin 2000), the Hα kernel motion, as observed in this event, is measured to infer the macroscopic electric field inside the RCS generated at the coronal reconnection point. We also investigate the role of such an electric field in accelerating X-ray– and microwave-emitting electrons through spectral analyses of X-ray observations from *Yohkoh* and microwave observations by OVSA. We obtain the following results:

1. Hα, hard X-ray, and microwave images all show two footpoints residing in and connecting the opposite magnetic polarities. During the impulsive phase, a flare footpoint kernel exhibits a systematic motion with a speed of 20–100 km s^{-1}. The two parts of the kernel divided by a light bridge show different motion patterns, one proceeding from relatively weak magnetic fields of $\sim$500 G into stronger fields of $\sim$900 G, and the other moving along the magnetic isogauss contour at $\sim$600 G.

2. According to the relation $E_c(t) = V_{\|}(t)B_n$ (Forbes & Priest 1984; Forbes & Lin 2000), we derive the electric field E_c in the coronal RCS using the measured velocity of the kernel motion $V_{\|}$ and the photospheric magnetic field B_n swept through by the motion. When comparing the evolution of the electric field with the $\leq$100 keV hard X-ray time profile, we find a correlation between the two curves during the rise of the major hard X-ray emission peak only for a kernel that moves along the magnetic field gradient. This result is partly in support of the general scenario of magnetic energy release via current dissipation inside the RCS.

3. The correlation between E_c and X-ray emission also suggests that $\leq$100 keV electrons are produced by a DC electric field acceleration mechanism (Litvinenko 1996). Given the observationally determined maximum electric field $E_c \approx 90$ V cm^{-1}, the acceleration length Δl must be about 10 m, which is 10^{-5} the full length l of the electric current sheet. This is possible with the presence of a nontrivial transverse magnetic field component $B_{\perp}$ at the reconnection point that quickly ejects the electrons out of the RCS after a short distance (Litvinenko 1996).

4. However, the temporal correlation between the inferred electric field and the hard X-rays is poor in other kernels, specifically, in the kernels that show either a motion along the isogauss region or no progressive motion at all. This could imply that the two-dimensional magnetic reconnection model involving the Hα kernel motion is not fully applicable to all part of the Hα kernels in the present event owing to its special magnetic geometry. Also, the microwaves have a different time profile and a much harder power spectrum than $\leq$100 keV X-rays. Since microwaves are produced by several hundred keV electrons, this finding suggests that there can be another acceleration mechanism to generate electrons in this energy range.

The authors thank Hugh Hudson for offering *Yohkoh* data and BBSO and OVSA observing staff for data support. The authors also thank the anonymous referee for valuable comments. This work is supported by the NSF grants AST 99-87366 and ATM-0086999, and NASA grants NRA-99-01-SSS-109 and NAG 5-9682.

REFERENCES

Benka, S. G., & Holman, G. D. 1994, ApJ, 435, 469
Brown, J. C. 1971, Sol. Phys., 18, 489
Canfield, R. C., & Gayley, K. G. 1987, ApJ, 322, 999
Cornwell, T., & Fomalont, E. B. 1999, in ASP Conf. Ser. 180, Synthesis Imaging in Radio Astronomy II, ed. G. B. Taylor, C. L. Carilli, & R. A. Perley (San Francisco: ASP), p. 10
Demoulin, P., Bagala, L. G., Mandrini, C. H., Hénoux, J. C., & Rovira, M. G. 1997, A&A, 325, 305
Demoulin, P., Hénoux, J. C., Priest, E. R., & Mandrini, C. H. 1996, A&A, 308, 643
Demoulin, P., Mandrini, C. H., Rovira, M. G., Hénoux, J. C., & Machado, M. E. 1994, Sol. Phys., 150, 221
Dreicer, H. 1959, Phys. Rev., 115, 238
Dulk, G. A., & Marsh, K. A. 1982, ApJ, 259, 350
Falchi, A., Qiu, J., & Cauzzi, G. 1997, A&A, 328, 371
Forbes, T. G., & Acton, L. W. 1996, ApJ, 459, 330
Forbes, T. G., & Lin, J. 2000, J. Atmos. Sol-Terr. Phys., 62, 1499
Forbes, T. G., & Priest, E. R. 1984, in Solar Terrestrial Physics: Present and Future, ed. D. M. Butler & K. Papadupoulous (NASA), 1
Foukal, P. V., & Behr, B. B. 1995, Sol. Phys., 156, 293
Gayley, K. G., & Canfield, R. C. 1991, ApJ, 380, 660
Högbom, J. A. 1974, A&AS, 15, 417
Holman, G. D. 1985, ApJ, 293, 584
Kitahara, T., & Kurokawa, H. 1990, Sol. Phys., 125, 321
Kopp, R. A., & Pneuman, G. W. 1976, Sol. Phys., 50, 85
Kosugi, T., Dennis, B. R., & Kai, K. 1988, ApJ, 324, 1118
Kurt, V. G., Akimov, V. V., Hagyard, M. J., & Hathaway, D. H. 2000, in ASP Conf. Ser. 206, High Energy Solar Physics: Anticipating HESSI, ed. R. Ramaty & N. Ramaty (San Francisco: ASP), 426
Lin, R. P., & Hudson, H. S. 1976, Sol. Phys., 50, 153
Litvinenko, Y. E. 1996, ApJ, 462, 997
Litvinenko, Y. E., & Craig, I. J. D. 2000, ApJ, 544, 1101
Mandrini, C. H., Demoulin, P., Rovira, M. G., & de La Beaujardiere, J.-F., & Hénoux, J. C. 1995, A&A, 303, 927
Mandrini, C. H., Rovira, M. G., Demoulin, P., Hénoux, J. C., Machado, M. E., & Wilkinson, L. K. 1993, A&A, 272, 609
Nitta, N., & Kosugi, T. 1986, Sol. Phys., 105, 73
Poletto, G., & Kopp, R. A. 1986, in The Lower Atmosphere of Solar Flares, ed. D. F. Neidig (Sunspot: NSO/Sacramento Peak), 453
Qiu, J., Ding, M. D., Wang, H., Gallagher, P. T., Sato, J., Denker, C., & Goode, P. R. 2001, ApJ, 554, 445
Raulin, J.-P., Vilmer, N., Trottet, G., Nitta, N., Silva, A. V. R., Kaufmann, P., Correia, E., & Magun, A. 2000, A&A, 355, 355
Sakao, T. 1994, Ph.D. thesis, Univ. Tokyo

Sato, J., Kosugi, T., & Makishima, K. 1999, PASJ, 51, 127
Sato, J., Sawa, M., Masuda, S., Sakao, T., Kosugi, T., & Sekiguchi, H. 1998, The *Yohkoh* HXT Image Catalogue (Nobeyama: Nobeyama Radio Obs./Natl. Astron. Obs.)
Schmieder, B., Forbes, T. G., Malherbe, J. M., & Machado, M. E. 1987, ApJ, 317, 956
Silva, A. V. R., Wang, H., & Gary, D. E. 2000, ApJ, 545, 1116
Švestka, Z. 1989, Sol. Phys., 121, 399
Švestka, Z., & Cliver, E. W. 1992, in Eruptive Solar Flares, ed. Z. Švestka et al. (Berlin: Springer), 1
Trottet, G., Rolli, E., Magun, A., Barat, C., Kuznetsov, A., Sunyaev, R., & Terekhov, O. 2000, A&A, 356, 1067
Wang, H., Qiu, J., Denker, C., Spirock, T., Chen, H., & Goode, P. R. 2000, ApJ, 542, 1080